

THE OFFICIAL MAGAZINE OF THE OCEANOGRAPHY SOCIETY

# Oceanography

CITATION

Zhao, Z., M.H. Alford, and J.B. Girton. 2012. Mapping low-mode internal tides from multisatellite altimetry. *Oceanography* 25(2):42–51, <http://dx.doi.org/10.5670/oceanog.2012.40>.

DOI

<http://dx.doi.org/10.5670/oceanog.2012.40>

COPYRIGHT

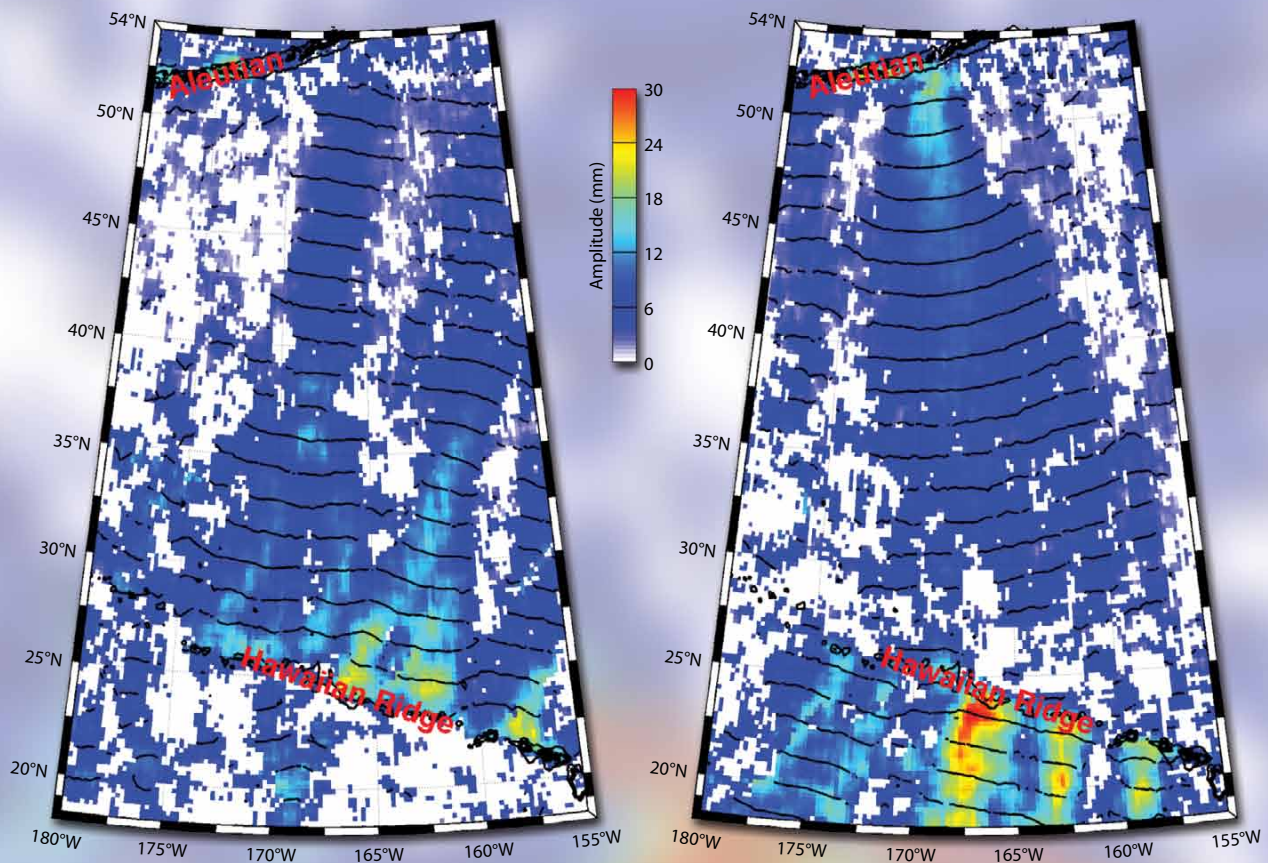
This article has been published in *Oceanography*, Volume 25, Number 2, a quarterly journal of The Oceanography Society. Copyright 2012 by The Oceanography Society. All rights reserved.

USAGE

Permission is granted to copy this article for use in teaching and research. Republication, systematic reproduction, or collective redistribution of any portion of this article by photocopy machine, reposting, or other means is permitted only with the approval of The Oceanography Society. Send all correspondence to: [info@tos.org](mailto:info@tos.org) or The Oceanography Society, PO Box 1931, Rockville, MD 20849-1931, USA.

# Mapping Low-Mode Internal Tides from Multisatellite Altimetry

BY ZHONGXIANG ZHAO, MATTHEW H. ALFORD, AND JAMES B. GIRTON



Coherent mode-1  $M_2$  internal tidal beams from the Hawaiian and Aleutian ridges, estimated from multisatellite altimetry by a plane-wave fit technique. The colors denote amplitude, and the black contours are phase lines (at an interval of one wavelength) for the largest northbound (left panel) or southbound (right panel) waves. White patches indicate regions of poor fits and/or amplitudes less than 3 mm (see the color bar).

**ABSTRACT.** Low-mode internal tides propagate over thousands of kilometers from their generation sites, distributing tidal energy across the ocean basins. Though internal tides can have large vertical displacements (often tens of meters or more) in the ocean interior, they deflect the sea surface only by several centimeters. Because of the regularity of the tidal forcing, this small signal can be detected by state-of-the-art, repeat-track, high-precision satellite altimetry over nearly the entire world ocean. Making use of combined sea surface height measurements from multiple satellites (which together have denser ground tracks than any single mission), it is now possible to resolve the complex interference patterns created by multiple internal tides using an improved plane-wave fit technique. As examples, we present regional  $M_2$  internal tide fields around the Mariana Arc and the Hawaiian Ridge and in the North Pacific Ocean. The limitations and some perspective on the multisatellite altimetric methods are discussed.

### INTERNAL TIDES

About 1 TW ( $10^{12}$  W) of power is lost from the surface tide in the deep ocean at rough bottom topography such as seamounts, ridges, and trenches (Egbert and Ray, 2000, 2001). A major fraction ( $\sim 80\%$ ) of the power is converted into low-mode internal tides (i.e., internal waves of tidal frequency and long vertical wavelengths; see Figure 1) and transported thousands of kilometers from the generation sites (Dushaw et al., 1995; Ray and Cartwright, 2001; Alford, 2003; Zhao and Alford, 2009). Internal tides may dissipate upon encountering strongly sheared currents, scattering on the rough seafloor, and cascading to small-scale waves through processes such as parametric subharmonic instability (PSI; e.g., St. Laurent and Garrett, 2002; Kunze and Llywellyn Smith, 2004; MacKinnon and Winters, 2005; Alford et al., 2007). The portion that does not dissipate via one of these mechanisms is thought to do so when it encounters distant continental slopes (e.g., Nash et al., 2007). The role of these mechanisms in the eventual dissipation of internal tides remains an open question. The geographic distribution of tidal energy dissipation is important for

large-scale ocean circulation, climate, and biological productivity (Munk and Wunsch, 1998; St. Laurent and Garrett, 2002). Thus, mapping internal tides from their generation sites to their dissipation sites may advance our knowledge of their dynamics. Internal tides are traditionally measured by in situ observations of their velocity and displacement profiles (Wunsch 1975; Alford 2003). However, the sparse distribution of these measurements limits in-depth knowledge of the internal tide field, particularly on a global scale.

### INTERNAL TIDES IN A ROTATING STRATIFIED OCEAN

Ocean stratification is described by the buoyancy frequency profile

$$N(z) = \left( -\frac{g}{\rho_0} \frac{d\rho(z)}{dz} \right)^{1/2},$$

where  $g$  is gravitational acceleration,  $\rho_0$  is a reference ocean water density,  $\rho(z)$  is potential density, and  $z$  is vertical coordinate (positive upward). An internal tide in a continuously stratified ocean can be represented by a sum of discrete baroclinic modes that depend only on the buoyancy frequency profile  $N(z)$  and the water depth  $H$ . The modes

are then described by the eigenvalue equation (Gill, 1982):

$$\frac{d^2\Phi(z)}{dz^2} + \frac{N^2(z)}{c_n^2} \Phi(z) = 0, \quad (1)$$

subject to rigid-lid boundary conditions  $\Phi(0) = \Phi(H) = 0$ , where  $\Phi(z)$  is the eigenfunction and  $c_n$  the eigenvalue for the  $n^{\text{th}}$  mode. The term  $\Phi(z)$  describes the baroclinic modal structures for displacement and vertical velocity;  $\Pi(z)$  describes the equivalent structures for horizontal velocity and pressure and is related to  $\Phi(z)$  via

$$\Pi(z) = \rho_0 c_n^2 \frac{d\Phi(z)}{dz}.$$

The effect of Earth's rotation is described by the local inertial frequency  $f = 2\Omega \sin(\text{latitude})$ , where  $\Omega (= 7.3 \times 10^{-5} \text{ rad s}^{-1})$  is Earth's rotation rate. The phase velocity  $c_p$  can be obtained as

$$c_p = \frac{\omega}{\sqrt{\omega^2 - f^2}} c_n,$$

where  $\omega$  is the tidal frequency (Rainville and Pinkel, 2006).

Typically, we solve Equation 1 for the four lowest baroclinic modes in a stratified deep ocean (Figure 1a). The normalized  $\Phi(z)$  and  $\Pi(z)$  (Figure 1b,c, respectively) have wavelengths 154, 77, 52, and 40 km for modes 1–4, respectively. While the barotropic tide may have wavelengths of thousands of kilometers, internal tidal wavelengths are much shorter.

Though the rigid-lid approximation is used to solve the eigenvalue equation,  $\Phi(z)$  is not zero at the sea surface. Via their pressure fluctuations  $\Pi(z)$  at the sea surface (Figure 1c), internal tides deflect the sea surface by several centimeters. Taking Figure 1 as an example, for a 10 m maximum internal amplitude, the sea surface amplitudes are 1.8, 0.6, 0.4, and 0.2 cm for modes 1–4, respectively. Lower

modes have greater sea surface amplitude for the same interior amplitude.

Conversely, the interior amplitude can be estimated from the sea surface amplitude. Thus, energy and flux can be calculated and are proportional to amplitude squared. From the hydrographic profiles, the vertical structures and propagation speeds of low-mode internal tides can be determined in the world ocean (Rainville and Pinkel, 2006). In addition, the functional relations from sea surface amplitude to energy and flux can be determined (Chiswell, 2006; Zhao and Alford, 2009).

The internal tidal frequency must be greater than the local near-inertial frequency, that is,  $\omega \geq f$ . For the diurnal and semidiurnal internal tides, this requirement gives rise to “turning latitudes” of about 29° and 75°, respectively. Progressive internal tides do not exist

in the open ocean poleward of turning latitudes (Dushaw, 2006; Rainville and Pinkel, 2006), although topographically trapped solutions may exist (e.g., Dale et al., 2001).

### INTERNAL TIDES FROM SATELLITE ALTIMETRY

Sea surface height (SSH) variations induced by internal tides have long been observed as tidal “cusps” around discrete tidal lines in frequency spectra (Munk and Cartwright, 1966; Colosi and Munk, 2006). However, exploring these weak signals over basin scales only became practical with the advent of satellite altimetry (Ray and Mitchum, 1996, 1997). Satellite altimetry can measure SSH with an accuracy of about 2 cm. Its measurement errors  $\sigma$  are distributed over a wide range of the spectrum. Therefore, to extract tidal

signals (with their precisely known frequencies), the errors scale as  $\sigma/\sqrt{N}$ , where  $N$  is the number of measurements. Thus, with a sufficient number (several hundreds) of measurements, satellite altimetry may resolve tidal signals with 1–2 mm resolution.

The orbit parameters of satellite altimeters are such that they repeat their ground tracks at intervals of tens of days (Table 1), periods much longer than the semidiurnal and diurnal tidal periods (0.5 and 1 day). This aliases tidal signals to long periods that are different for each altimeter. For example, for the TOPEX/Poseidon (T/P) altimeter,  $M_2$  and  $S_2$  tides alias to 62.11 and 58.74 days, respectively. It is remarkable that internal tides can be studied with a dataset exhibiting sampling only once every 20–60 wave periods. Harmonic analysis over many samples is used to extract the signal at each tidal frequency. The method relies on the coherence of internal tides such that phase is largely maintained from sample to sample. It is only this temporally coherent portion of the signal that is detectable by altimetry, a point we return to later.

**Zhongxiang Zhao** (zzhao@apl.washington.edu) is Senior Oceanographer, Applied Physics Laboratory, University of Washington, Seattle, WA, USA. **Matthew H. Alford** is Principal Oceanographer, Applied Physics Laboratory, and Associate Professor, School of Oceanography, University of Washington, Seattle, WA, USA. **James B. Girton** is Senior Oceanographer, Applied Physics Laboratory, and Affiliate Assistant Professor, School of Oceanography, University of Washington, Seattle, WA, USA.

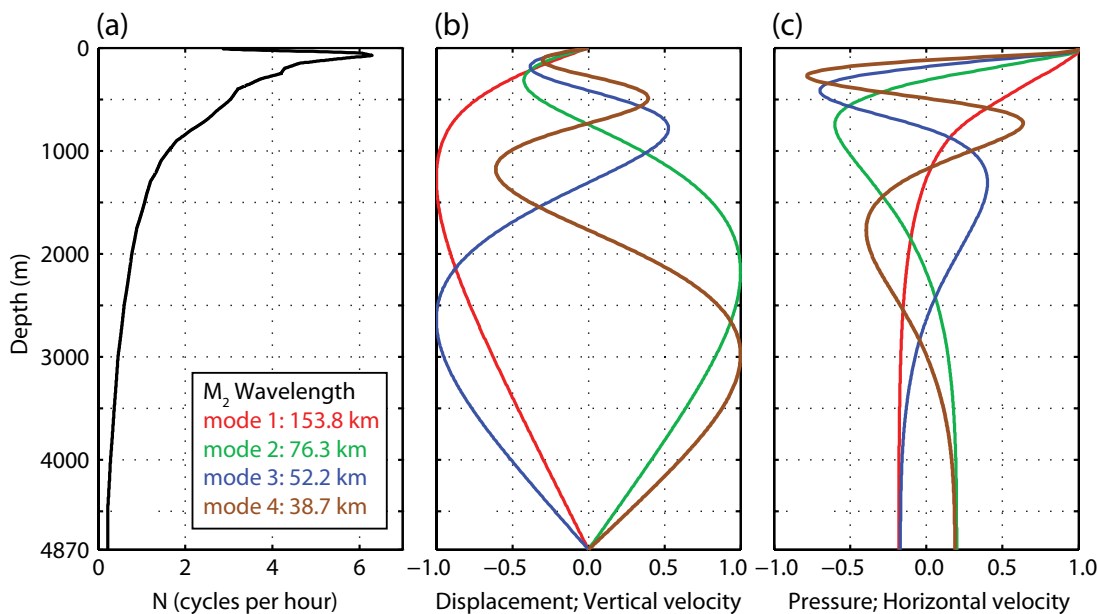


Figure 1. (a) Buoyancy frequency profile at 25.5°N, 195°E from the World Ocean Atlas database. The four lowest baroclinic modes are solutions of Equation 1. (b) Normalized baroclinic modal structures for displacement and vertical velocity. (c) Normalized baroclinic modal structures for horizontal velocity and pressure. The wave-lengths of modes 1–4  $M_2$  internal tides are given.

The accuracy and longevity of T/P relative to its contemporary altimeters (e.g., Seasat and Geosat) made it the instrument of choice for early internal tide studies. The continued success of the European Remote Sensing (ERS) and Geosat Follow-On (GFO) have resulted in complementary datasets long enough to detect internal tides (Zhao et al., 2011).  $M_2$  and  $O_1$  tides are now extracted on all four track patterns (Table 1). But the sun-synchronous ERS orbit cannot detect the  $S_2$  and  $K_1$  tides because  $S_2$  aliases to an infinitely long period and  $K_1$  to the annual cycle (Le Provost, 2001).

Zhao et al. (2011) report that the  $M_2$  internal tides extracted from T/P, ERS, and GFO agree with each other very well at crossover points. This observation suggests that the datasets may be combined to improve the spatial resolution. However, some satellite altimeter datasets (both old and new) are still incompatible and cannot be incorporated. Early altimetric data from the 1970s and 1980s (Skylab, SEASAT, and Geosat) were not suitable for the study of internal tides, either because of track

determination errors, short duration, or limitations in SSH measurement accuracy. Cryosat-2 (launched April 2010) has a long repeat period of one year (allowing about 7,000 ground tracks), and therefore will never make enough repeats for tidal analysis. HY-2A, another new altimeter, may one day be useful for internal tide studies but is not following the track pattern of any existing altimeters; it will take ~ 10 years to build up enough samples.

The harmonically extracted tidal signals contain SSH variations caused by both barotropic and baroclinic tides. They are of the same frequency but different wavelengths. There are two methods to separate them. (1) A high-pass filter can be used to remove barotropic tidal signals along each track. Internal tides with large angle to ground tracks, however, may have long apparent wavelengths, and thus cannot be separated from the barotropic tide. (2) Barotropic tidal models may also be used to separate the signals. State-of-the-art tidal models, however, still have errors of about two centimeters in the deep ocean (Ray et al.,

2011), which is of the same order as baroclinic tides. Thus, the barotropic tidal residuals may cause some confusion.

Since Ray and Mitchum (1996, 1997) first demonstrated that SSH fluctuations caused by internal tides can be detected by satellite altimetry, the method has been used to study internal tides around the Aleutian Ridge (Cummins et al., 2001), near New Zealand in the southern Pacific Ocean (Chiswell, 2006), near the Kerguelen Plateau in the southern Indian Ocean (Maraldi et al., 2011), and across the entire globe (Kantha and Tierney, 1997; Tian et al., 2006).

### ALONG-TRACK ANALYSIS

Point-wise harmonic analysis is a standard method for extracting the constituents of predetermined frequency. The method has been widely used to extract internal tides from T/P altimeter data. At every point along one T/P track, a time series of SSH measurements is analyzed. Harmonic analysis uses a standard least squares method to determine the amplitude and phase. But the time series should be long enough to separate

Table 1. Satellite altimeter data: TOPEX/Poseidon (T/P), Jason-1 (J1), Jason-2 (J2), Geosat Follow-on (GFO), European Remote Sensing (ERS)

Dataset	Satellite Altimeter	Repeat Period (day)	Total Tracks	Track Spacing (km)*	Data Period (mm/yyyy)	Tidal Resolvability			
						$M_2$	$S_2$	$O_1$	$K_1$
T/P-J1-J2	T/P	9.9156	254	315	10/1992–08/2002	Yes	Yes	Yes	Yes
	J1				02/2002–01/2009				
	J2				07/2008–now				
T/Pt-J1t	T/P tandem	17.0505	488	164	10/2002–10/2005	Yes	Yes	Yes	Yes
	J1 tandem				02/2009–now				
GFO	GFO	17.0505	488	164	10/2000–03/2008	Yes	Yes	Yes	Yes
ERS	ERS-1	35	1002	80	10/1992–12/1993	Yes	No**	Yes	No***
	ERS-2				05/1995–06/2003				
	Envisat				07/2003–10/2010				

\*track spacing at the equator; \*\*alias to infinity period; \*\*\*alias to annual period

different tidal frequencies. For example, 110 T/P measurements (i.e., three years of operation) are needed to separate the  $M_2$  and  $S_2$  tides (Le Provost, 2001). However, 6.6 and 8.7 years of ERS and GFO data are required to extract  $M_2$  tides from these datasets, because ERS and GFO have different aliasing periods (Zhao et al., 2011).

As an example, Figure 2 shows  $M_2$  internal tides along T/P-J1-J2 track 249 extracted by harmonic analysis. The harmonically fitted  $M_2$  internal tides are shown as black lines. Before harmonic analysis, a high-pass filter ( $< 1,000$  km) is applied to remove the barotropic tidal residuals. Thus, the results contain internal tides of all modes. To support this point, the along-track ( $10\text{--}40^\circ\text{N}$ ) wavenumber spectrum of  $M_2$  harmonics is calculated (Figure 2d, black line). On the spectrum, there are several discrete spectral peaks, which correspond to the mode 1–4 signals.  $M_2$  internal tides of different modes have different

wavelengths (see Figure 1). Their theoretical wavenumbers (inverse of wavelengths) agree well with the observed spectral peaks (Figure 2d, vertical lines).

Band-pass filters are used to separate internal tidal signals into various modes according to their wavelengths. In this case, the cut-off wavelengths for modes 1–3 are [100 500], [60 120], and [45 65] km, respectively. Spectra of the band-pass filtered components are shown in Figure 2d (colored curves). For modes 1–2, the band-pass filtered results are in agreement with the raw results, suggesting the band-pass filter works very well. However, the extracted mode-3 component is slightly lower, likely due to its narrower filter window (restricted by the fact that it is close to the mode-4 wavelength, 38.7 km).

Amplitude and phase harmonically extracted from the band-pass filtered mode-1  $M_2$  internal tides are shown as red lines in Figures 2a and 2b, respectively. The increasing phase suggests that

the  $M_2$  internal tides are propagating away from the Hawaiian Ridge. Thus, its along-track wavelength can be estimated. However, there exist half-wavelength variations in amplitude (Figure 2a, red line). Zhao and Alford (2009) developed a variation on the harmonic analysis method, allowing separation of waves traveling in different directions. Instead of processing at single locations, the method uses data within one wavelength along a track, and fits progressive waves. Internal tides are thus extracted in two opposing directions along the track. In Figure 2a,b, the mode-1 northward progressive  $M_2$  internal tides are shown in blue (the southward component is not shown here). The results explain the originally puzzling half-wavelength variations in harmonic amplitude and phase. The half-wavelength variations are found to be a consequence of the interference pattern between waves traveling in opposite directions. When separated, amplitude and phase much more closely

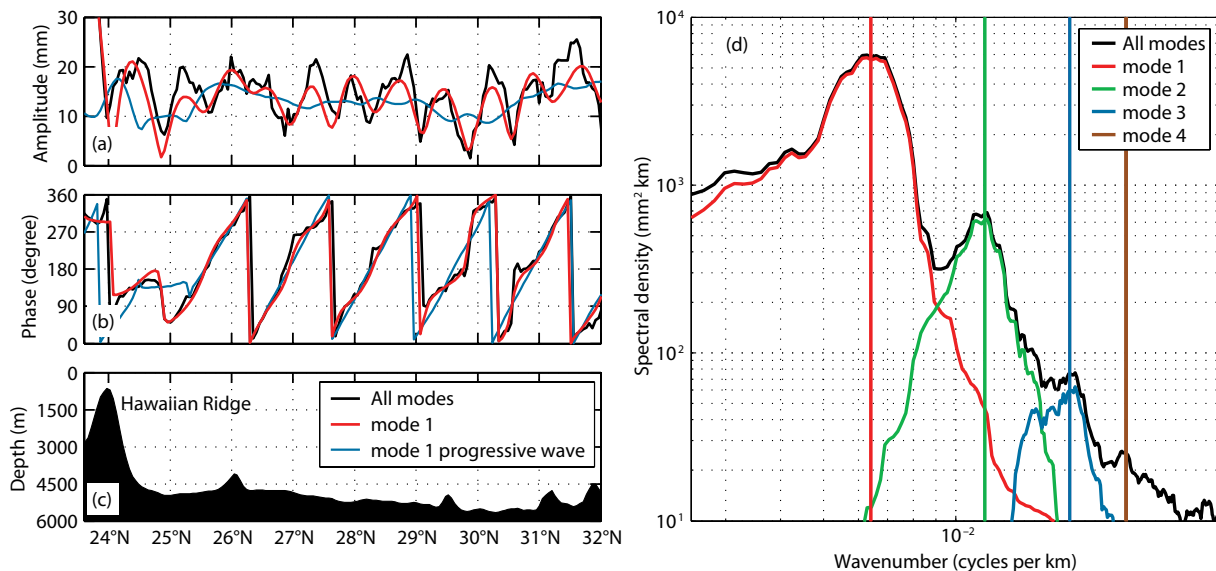


Figure 2.  $M_2$  internal tides along TOPEX/Poseidon-Jason-1-Jason-2 (T/P-J1-J2) track 249. (a) Amplitude. (b) Phase. In (a, b), the black lines denote  $M_2$  internal tides containing all modes; the red lines denote the band-pass filtered ([100 500] km) mode-1 signals; the blue lines denote the mode-1 progressive internal tides radiating away from the Hawaiian Ridge. (c) Along-track bottom topography. (d) Along-track wavenumber spectra of the harmonically extracted  $M_2$  tidal constituents ( $10\text{--}40^\circ\text{N}$ ). In (d), the black lines represent the  $M_2$  components with high-pass filter ( $< 1,000$  km). The red, green, and blue lines indicate spectra of the band-pass filtered components for modes 1 ([100 500] km), 2 ([60 120] km), and 3 ([45 65] km), respectively. The vertical lines label the spectral peaks of mode-1 (160 km), -2 (80 km), -3 (52 km), and -4 (40 km)  $M_2$  internal tides.

resemble progressive waves. In Figure 2b, the northward-propagating mode-1  $M_2$  internal tides show a clear linear phase increase and smoother amplitude, allowing better estimates of their energetics and propagation.

## TWO-DIMENSIONAL PLANE-WAVE FIT

The along-track analysis described above is a powerful tool for illustrating the existence of internal tidal waves that happen to propagate nearly parallel to the satellite's tracks. However, it is clearly of limited generality in an ocean with an arbitrary number of waves propagating in arbitrary directions. One proposed way forward has been to construct an inverse solution for a beam pattern based on a continuum of waves over a large area of ocean (Dushaw, 2002; Dushaw et al., 2011), but this approach ignores the spatial inhomogeneity of energy sources and sinks. Instead, Ray and Cartwright (2001) developed a local plane-wave fit technique using the altimeter grid over a small region—analogueous to using a cluster of moorings as an antenna to detect propagating wave signals (Hendry, 1977; Zhao and D'Asaro, 2011). They then used this method to present the first altimetric map of the  $M_2$  internal tide around the Hawaiian Ridge. Zhao and Alford (2009) refined Ray and Cartwright's (2001) method to resolve multiple waves.

The plane-wave fit technique uses the SSH measurements at all data points in one region from several neighboring ground tracks. In each radial direction, a single best-fit wave (amplitude and phase) can be determined. Its frequency is known (the tidal constituent, e.g.,  $M_2$  or  $S_2$ ) and its wavelength is known from the baroclinic eigenvalue equation (Equation 1), given a stratification profile, water depth, and latitude. When

the fitted amplitude is plotted versus compass direction, a wave appears as a lobe (Figure 3).

The plane-wave fit technique is limited by the density of the satellite ground tracks relative to the internal tide wavelength (Ray and Cartwright, 2001). The fitting region must be big enough to contain several neighboring tracks as well as to span a significant fraction of the wave, but smaller fitting windows are better able to resolve structures in the internal tide field. In addition, the presence of multiple internal tides requires higher resolution to resolve the resultant complicated patterns. Multisatellite altimetry allows smaller fitting windows to be used. As Figure 3 shows, waves with windows smaller than 240 km on a side cannot be identified using data from a single altimeter, but with four sets of ground

tracks, waves can be separated with smaller fitting windows. Importantly, the fitted amplitudes in smaller fitting regions are also greater than those from bigger fitting regions. But there is a trade-off between spatial resolution and directional resolution (Zhao et al., 2011). As known from antenna theory, the smaller the fitting region, the poorer the angular resolution (Hendry, 1977).

Multiple internal tides may exist in one given region and cause complicated interference patterns (Rainville et al., 2010; Zhao et al., 2010). These waves must be resolved separately to interpret their propagation and energetics accurately (Alford and Zhao, 2007). The improved plane-wave fit technique may resolve multiple waves. For the location shown in Figure 3d, there are two outstanding lobes corresponding to the two

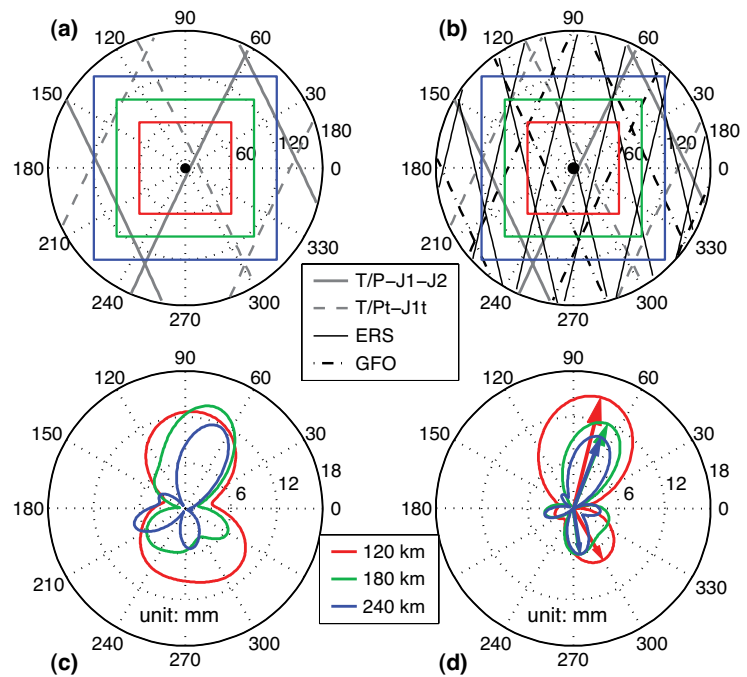


Figure 3. An example of the plane-wave fit technique around 33.5°N, 199°E (black dots). (a) Ground tracks of T/P-J1-J2 and T/Pt-J1t ( $t = \text{tandem}$ ). (b) Ground tracks of T/P-J1-J2, T/Pt-J1t, ERS, and GFO. (c, d) Radial amplitude of mode-1  $M_2$  internal tides plotted versus direction, obtained using different datasets in (a) and (b), respectively. The colored boxes in (a, b) denote the sizes of the fitting regions, and the colored curves in (c, d) denote the fitted amplitudes. In (d), the arrows indicate the northeastward and southeastward Hawaiian and Aleutian beams. Adapted from Zhao et al. (2011)

internal tide beams originating from the Hawaiian and Aleutian ridges (see figure on page 44).

Due to the irregular distribution of ground tracks, some lobes may be artifacts of the antenna rather than actual waves. The biggest of these “side lobes” in the multisatellite calculations may reach to 20% of the main wave (Zhao et al., 2011). To minimize the impact of the side lobes on the solutions for waves traveling in other directions, an iterative procedure is used (Figure 4). First, the amplitude, phase, and direction of the wave with the greatest amplitude are determined from the raw signals (Figure 4b, blue arrow). A plane wave with these parameters is then generated (blue curve) and subtracted from the raw data (green). This step has the effect of removing both the wave and its side lobes from the signals. The procedure can then be repeated for as

many waves as desired. In practice, only two or three waves generally dominate the signals (Figure 4c,d). Once these waves are determined, the entire procedure is repeated for each wave with the other waves subtracted (Figure 4, red, green, and brown arrows). This procedure improves the result because the side lobes of the other waves are removed while computing the solution for each wave. Note that the final computed waves (Figure 4f, colored arrows) differ slightly from the initial ones (black arrows).

## REGIONAL RESULTS

### Mariana Arc

The Mariana Arc approximates an arc of a circle 630 km in radius centered at 17°N, 139.6°E (Figure 5, black curve). Examples of the plane-wave fit technique are shown in 16 fitting windows of 160 km on a side (Zhao and D’Asaro,

2011; Figure 5a). The results reveal that internal tides are generally in the east–west direction. Note that previous studies have focused mainly on internal tides in the south–north direction because they are closer to the track direction. This example confirms that the phase variation across multiple tracks allows for the robust extraction of eastward and westward waves.

The westward-propagating  $M_2$  internal tides from the Mariana Arc converge at its center (Figure 5b). In the focal region centered at 17°N, 139.6°E, the spatially smoothed energy flux is about  $6.5 \text{ kW m}^{-1}$ , about four times the along-arc mean value, while the spatially unsmoothed energy flux may reach up to  $17 \text{ kW m}^{-1}$ , comparable to the value at the Hawaiian Ridge (Zaron et al., 2009).  $M_2$  internal tides converge in a focal region of a size comparable to that of a perfect focus (Figure 5c).

### Hawaiian Ridge

A clear view of the  $M_2$  internal tides around the Hawaiian Ridge is provided by the high spatial resolution of multisatellite altimetry (Zhao et al., 2011). The resultant mode-1 and -2 energy fluxes emanating from the Hawaiian Ridge are illustrated in Figure 6a and 6b, respectively. Discrete generation sites and internal tidal beams are distinguishable. Previous studies could only discern three generation sites: Nihoa Island (NI), Kauai Channel (KC), and French Frigate Shoals (FFS); now, more generation sites are resolved.  $M_2$  internal tidal energy fluxes estimated from multisatellite altimetry products are greater and agree better with model results than previous single satellite estimates (Ray and Cartwright, 2001). This agreement confirms that previous underestimates were partly due to the more widely spaced

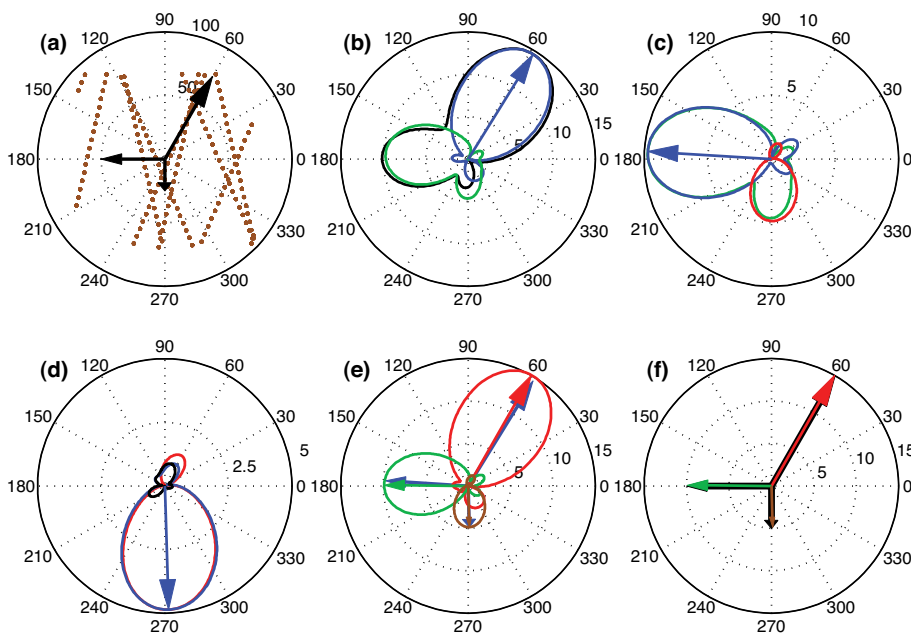


Figure 4. Illustration of the iterative plane-wave fit technique using synthetic data. (a) Data points within a 140 km window from a typical multiple satellite track pattern. Three  $M_2$  waves are created (black arrows). (b) Initially fitted amplitude (black) with the maximal lobe selected (blue arrow). The green line shows the fitted amplitude after removing the first wave (blue curve). (c) Repeat (b) to determine and remove the second wave. (d) Repeat (c) to determine and remove the third wave. The final residual is shown in black. (e) The three waves are readjusted by the plane-wave fit technique with the other two waves removed. The blue arrows denote these waves before the adjustment, while the red, green, and brown arrows denote waves after adjustment. (f) Comparisons of the real waves (black, from panel a) and the finally determined waves (colored).

ground tracks and consequent larger fitting region. The map of mode-2  $M_2$  internal tides also reveals that they are relatively weaker, mainly associated with rough topography such as the Hawaiian Ridge and the Musicians Seamounts. The signal is traceable over 500 km by the satellite altimetry (Figure 6b); it becomes undetectable mainly due to the fact that mode-2 loses coherence easily.

### The North Pacific Ocean

It is well known that the central North Pacific Ocean contains internal tides originating from the Hawaiian and Aleutian ridges (Ray and Cartwright, 2001; Zhao and Alford, 2009). By multi-satellite altimetry, the mode-1  $M_2$  internal tide field is obtained using the improved plane-wave fit technique (see figure on page 44), revealing northward and southward components. If the two beams were not resolved, their phase would form confusing interference patterns that could mask the signatures of individual sources. Our new results reveal that both beams propagate over 3,500 km across the North Pacific Ocean. The southward Aleutian beam spreads cylindrically. It is about 300 km wide at 50°N, and becomes 1,500 km wide at 35°N. The northward Hawaiian beam is actually composed of at least two distinct beams.

### LIMITATIONS AND CHALLENGES

#### Missing Incoherent Component

Satellite altimetry can only detect temporally coherent signals, potentially resulting in underestimation of the energy in the internal tide when either the generation or propagation of the waves changes in time—for example, due to mesoscale, seasonal, or interannual variability. Stratification and low-frequency currents affect the propagation of internal

tides, with a gradual loss of coherence expected due to propagation through a time-varying field of mesoscale eddies, making quantitative estimates of the flux at long range uncertain. Internal tide generation is also expected to vary in response to stratification changes at the major topographic features. Approaches for estimating these effects have included ray tracing through mesoscale eddy fields derived from altimetry (using an assumed vertical structure; Rainville and Pinkel, 2006), diagnosis of internal tide properties in time-varying tidal models (Arbic et al., 2010), and seasonal analysis of internal tides in the 20-year T/P-J1-J2 record (Ray and Zaron, 2011).

### Mesoscale Eddy Contamination

Internal tides alias to tens of days (e.g., 62.11 days for T/P  $M_2$ ), causing an overlap with the wide spectral band of mesoscale eddies. Because eddies also occupy a broad range of spatial scales, including the 100–200 km of internal tide wavelengths, there is potential for eddy signals (tens of centimeters in amplitude) to contaminate, or even overwhelm, detection of the internal tide. This is particularly likely in energetic regions, such as the Kuroshio, Gulf Stream, and Antarctic Circumpolar Circulation (ACC) systems (J. Richman, Oregon State University, *pers. comm.*, 2012). Ray and Byrne (2010) suggest a

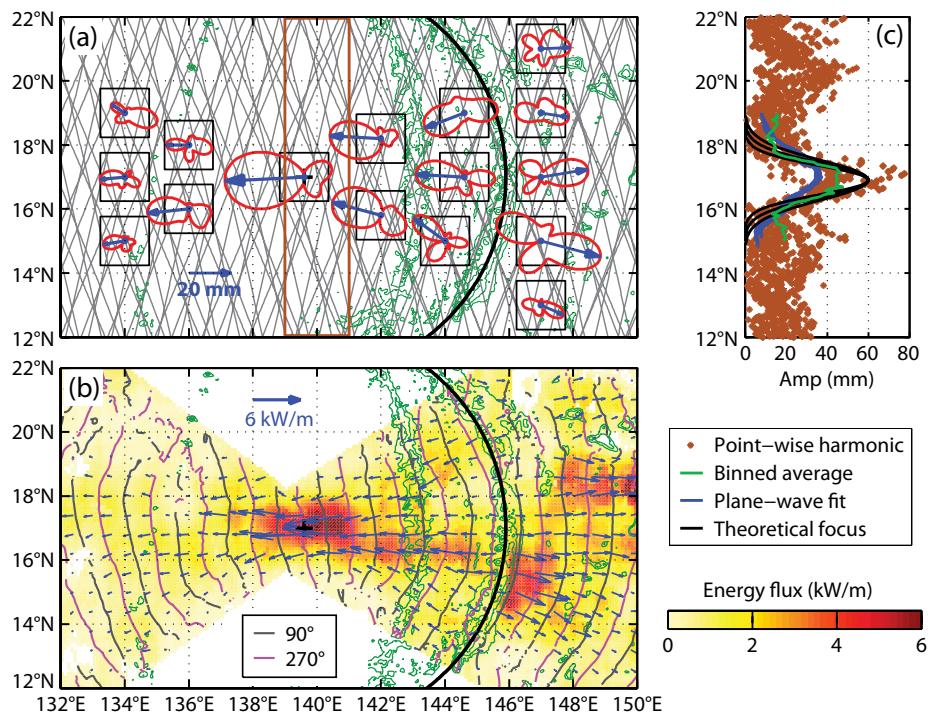


Figure 5.  $M_2$  internal tides around the Mariana Arc. (a) Examples of the plane-wave fit technique. The gray lines show the ground tracks of all satellite missions. The black boxes show the fitting regions (160 km  $\times$  160 km). The red curves show the plane-wave fitted amplitudes versus compass direction. The blue arrows indicate the selected internal tidal waves. (b)  $M_2$  internal tides. The yellow to red colors indicate the magnitudes of energy fluxes of  $M_2$  internal tides. The blue arrows indicate the energy flux vectors. The isophase lines of 90° and 270° are shown in gray and magenta, respectively. In both (a) and (b), the ideal Mariana Arc and its center are shown by a black curve and a black cross, respectively; the bathymetric contours at 1,000, 2,000, and 3,000 m are shown in green. (c) Amplitudes of  $M_2$  internal tides plotted versus latitude in the focal region (a, brown box): point-wise harmonic analysis (brown dots), 0.06° binned average of the point-wise harmonic analysis (green), and plane-wave fit (blue). The black lines show three theoretical focal sizes with radii of 100, 120, and 140 km (representing the range of uncertainty in the geometrical parameters), and amplitudes normalized to 60 mm. Adapted from Zhao and D'Asaro (2011)

cure for this contamination through the use of the “other” multisatellite product: the time-averaged and gridded AVISO maps of mesoscale SSH. By subtracting these maps prior to harmonic analysis for internal tides, they make use of the anti-aliasing aspects of multisatellite altimetry: while aliased internal tides may contaminate some aspects of the mesoscale maps, the smoothing over multiple tracks removes the time-coherent signal present in each altimeter. They report that this method works well in the ACC region off South Africa, setting the stage for its use in other energetic regions.

## PERSPECTIVE

### Assimilation to Numerical Models

Increasing computational power is approaching the capability to simulate the global internal tide field (Simmons et al., 2004; Arbic et al., 2010; Egbert et al., 2012). Field measurements for the validation of these models are scarce and sometimes hard to interpret due to complex interference patterns, making altimetric results a key component of

future modeling efforts. Though satellite altimetry may underestimate their amplitude, the phase of internal tides is very well defined (see Figure 10 in Zhao et al., 2011) and may be a robust benchmark for models.

### SWOT Satellite Altimetry

Direct observations of internal tides will receive a huge boost from the Surface Water and Ocean Topography (SWOT) wide-swath altimeter, which will provide real two-dimensional observations of SSH at  $\sim 5$  km spatial resolution, far superior to the current neighboring ground tracks of multiple satellites (Fu et al., 2010). The planned accuracy is expected to allow the detection of significantly smaller-scale high-mode components than the first four described here and will enable an unprecedented view of the internal tide generation and dissipation sites. With a 100 km wide swath, average revisit times will depend on latitude, with two to four revisits at low to mid latitudes and up to 10 revisits at high latitudes per  $\sim 20$  day repeat

period (Fu et al., 2010; Durand et al., 2010). These revisits may help loosen the limitations of harmonic analysis, but several years of data accumulation will still be required before internal tides can be extracted.

## ACKNOWLEDGMENTS

Z. Zhao and M.H. Alford were supported by NSF grants OCE-1029268 and OCE-1129129. J.B. Girton was supported by ONR grant N00014-08-1-0983. The altimeter products were produced by Ssalto/Duacs and distributed by AVISO, with support from CNES (<http://www.aviso.oceanobs.com/duacs>). 

## REFERENCES

- Alford, M.H. 2003. Redistribution of energy available for ocean mixing by long-range propagation of internal waves. *Nature* 423:159–162, <http://dx.doi.org/10.1038/nature01628>.
- Alford, H.M., J. MacKinnon, Z. Zhao, R. Pinkel, and T. Peacock. 2007. Internal waves across the Pacific. *Geophysical Research Letters* 37, L24061, <http://dx.doi.org/10.1029/2007GL031566>.
- Alford, M.H., and Z. Zhao. 2007. Global patterns of low-mode internal-wave propagation. Part II: Group velocity. *Journal of Physical Oceanography* 37:1,849–1,858, <http://dx.doi.org/10.1175/JPO3086.1>.

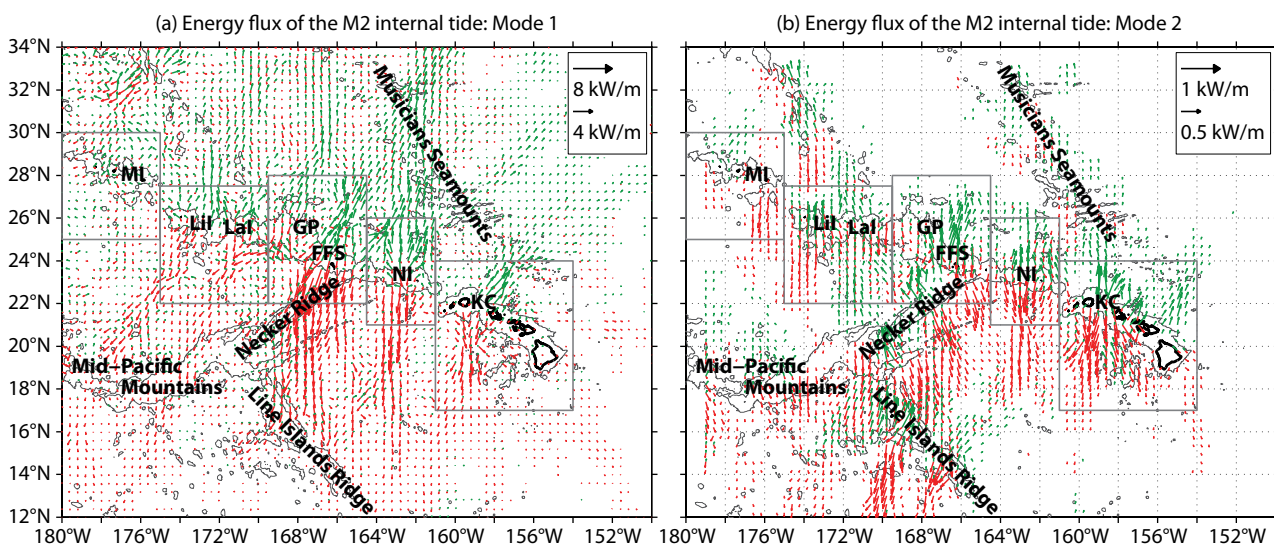


Figure 6. (a) Energy flux of mode-1  $M_2$  internal tides around the Hawaiian Ridge, estimated from multisatellite altimetry using a 120 km fitting region. The 4,000 m isobath contours are shown in gray. Remarkable generation sites are labeled: Midway Island (MI), Lisianski Island (Lil), Laysan Island (Lal), Gardner Pinnacles (GP), French Frigate Shoals (FFS), Nihoa Island (NI), and Kauai Channel (KC). Red and green arrows indicate southward and northward internal tides, respectively. Flux arrows smaller than  $0.15 \text{ kW m}^{-1}$  are not plotted. (b) Mode-2  $M_2$  internal tides. Flux arrows smaller than  $0.05 \text{ kW m}^{-1}$  are not plotted. Adapted from Zhao et al. (2011)

- Arbic, B.K., A.J. Wallcraft, and E.J. Metzger. 2010. Concurrent simulation of the eddy general circulation and tides in a global ocean model. *Ocean Modelling* 32:175–187, <http://dx.doi.org/10.1016/j.ocemod.2010.01.007>.
- Chiswell, S.M. 2006. Altimeter and current meter observations of internal tides: Do they agree? *Journal of Physical Oceanography* 36:1,860–1,872, <http://dx.doi.org/10.1175/JPO2944.1>.
- Colosi, J.A., and W. Munk. 2006. Tales of the venerable Honolulu tide gauge. *Journal of Physical Oceanography* 36:967–996, <http://dx.doi.org/10.1175/JPO2876.1>.
- Cummins, P.F., J.Y. Cherniawsky, and M.G.G. Foreman. 2001. North Pacific internal tides from the Aleutian Ridge: Altimeter observations and modeling. *Journal of Marine Research* 59:167–191.
- Dale, A.C., J.M. Huthnance, and T.J. Sherwin. 2001. Coastally-trapped waves and tides at near-inertial frequencies. *Journal of Physical Oceanography* 31:2,958–2,970, [http://dx.doi.org/10.1175/1520-0485\(2001\)031<2958:CTWATA>2.0.CO;2](http://dx.doi.org/10.1175/1520-0485(2001)031<2958:CTWATA>2.0.CO;2).
- Durand, M., L.L. Fu, D.P. Lettenmaier, D.E. Alsdorf, E. Rodriguez, and D. Esteban-Fernandez. 2010. The surface water and ocean topography mission: Observing terrestrial surface water and oceanic submesoscale eddies. *Proceedings of the IEEE* 98:766–779, <http://dx.doi.org/10.1109/JPROC.2010.2043031>.
- Dushaw, B.D. 2002. Mapping low-mode internal tides near Hawaii using TOPEX/POSEIDON altimeter data. *Geophysical Research Letters* 29, 1250, <http://dx.doi.org/10.1029/2001GL013944>.
- Dushaw, B.D. 2006. Mode-1 internal tides in the western North Atlantic Ocean. *Deep-Sea Research Part I* 53:449–473, <http://dx.doi.org/10.1016/j.dsr.2005.12.009>.
- Dushaw, B.D., B.M. Howe, B.D. Cornuelle, P.F. Worcester, and D.S. Luther. 1995. Barotropic and baroclinic tides in the central North Pacific Ocean determined from long-range reciprocal acoustic transmissions. *Journal of Physical Oceanography* 25:631–647, [http://dx.doi.org/10.1175/1520-0485\(1995\)025<0631:BABTTI>2.0.CO;2](http://dx.doi.org/10.1175/1520-0485(1995)025<0631:BABTTI>2.0.CO;2).
- Dushaw, B.D., P.F. Worcester, and M.A. Dzieciuch. 2011. On the predictability of mode-1 internal tides. *Deep-Sea Research Part I* 58(6):677–698, <http://dx.doi.org/10.1016/j.dsr.2011.04.002>.
- Egbert, G.D., S.Y. Erofeeva, and E.D. Zaron. 2012. Mapping M2 internal tides using a data-assimilative reduced gravity model. Paper presented at the Ocean Sciences Meeting, Salt Lake City, Utah, February 19, 2012, poster B2112.
- Egbert, G.D., and R.D. Ray. 2000. Significant dissipation of tidal energy in the deep ocean inferred from satellite altimeter data. *Nature* 405:775–778, <http://dx.doi.org/10.1038/35015531>.
- Egbert, G.D., and R.D. Ray. 2001. Estimates of M2 tidal energy dissipation from TOPEX/Poseidon altimeter data. *Journal of Geophysical Research* 106(C10):22,475–22,502, <http://dx.doi.org/10.1029/2000JC000699>.
- Fu, L.-L., D.B. Chelton, P.-Y. Le Traon, and R. Morrow. 2010. Eddy dynamics from satellite altimetry. *Oceanography* 23(4):14–25, <http://dx.doi.org/10.5670/oceanog.2010.02>.
- Gill, A.E. 1982. *Atmosphere-Ocean Dynamics*. Academic Press, 662 pp.
- Hendry, R.M. 1977. Observations of the semidiurnal internal tide in the western North Atlantic Ocean. *Philosophical Transactions of the Royal Society of London A* 286:1–26, <http://dx.doi.org/10.1098/rsta.1977.0108>.
- Kantha, L.H., and C.C. Tierney. 1997. Global baroclinic tides. *Progress in Oceanography* 40:163–178, [http://dx.doi.org/10.1016/S0079-6611\(97\)00028-1](http://dx.doi.org/10.1016/S0079-6611(97)00028-1).
- Kunze, E., and S.G. Llewellyn Smith. 2004. The role of small-scale topography in turbulent mixing of the global ocean. *Oceanography* 17(1):55–64, <http://dx.doi.org/10.5670/oceanog.2004.67>.
- MacKinnon, J.A., and K.B. Winters. 2005. Subtropical catastrophe: Significant loss of low-mode tidal energy at 28.9. *Geophysical Research Letters* 32, L15605, <http://dx.doi.org/10.1029/2005GL023376>.
- Maraldi, C., F. Lyard, L. Testut, and R. Coleman. 2011. Energetics of internal tides around the Kerguelen Plateau from modeling and altimetry. *Journal of Geophysical Research* 116, C06004, <http://dx.doi.org/10.1029/2010JC006515>.
- Le Provost, C. 2001. Ocean tides. Pp. 267–303 in *Satellite Altimetry and Earth Sciences: A Handbook for Technique and Applications*. L.-L. Fu and A. Cazenave, eds, Academic, San Diego, California.
- Munk, W.H., and D.C. Cartwright. 1966. Tidal spectroscopy and prediction. *Philosophical Transactions of the Royal Society of London A* 259:533–581, <http://dx.doi.org/10.1098/rsta.1966.0024>.
- Munk, W.H., and C. Wunsch. 1998. Abyssal recipes II: Energetics of tidal and wind mixing. *Deep-Sea Research Part I* 45:1,977–2,010, [http://dx.doi.org/10.1016/S0967-0637\(98\)00070-3](http://dx.doi.org/10.1016/S0967-0637(98)00070-3).
- Nash, J.D., M.H. Alford, E. Kunze, K. Martini, and S. Kelly. 2007. Hotspots of deep ocean mixing on the Oregon continental slope. *Geophysical Research Letters* 34, L01605, <http://dx.doi.org/10.1029/2006GL028170>.
- Rainville, L., T.M.S. Johnston, G.S. Carter, M.A. Merrifield, R. Pinkel, P.F. Worcester, and B.D. Dushaw. 2010. Interference pattern and propagation of the M2 internal tide south of the Hawaiian Ridge. *Journal of Physical Oceanography* 40:311–325, <http://dx.doi.org/10.1175/2009JPO4256.1>.
- Rainville, L., and R. Pinkel. 2006. Propagation of low-mode internal waves through the ocean. *Journal of Physical Oceanography* 36:1,220–1,236, <http://dx.doi.org/10.1175/JPO2889.1>.
- Ray, R.D., and D.A. Byrne. 2010. Bottom pressure tides along a line in the southeast Atlantic Ocean and comparisons with satellite altimetry. *Ocean Dynamics* 60:1,167–1,176, <http://dx.doi.org/10.1007/s10236-010-0316-0>.
- Ray, R.D., and D.E. Cartwright. 2001. Estimates of internal tide energy fluxes from TOPEX/Poseidon altimetry: Central North Pacific. *Geophysical Research Letters* 28:1,259–1,262, <http://dx.doi.org/10.1029/2000GL012447>.
- Ray, R.D., G.D. Egbert, and S.Y. Erofeeva. 2011. Tide predictions in shelf and coastal waters: Status and prospects. Pp. 191–216 in *Coastal Altimetry*. S. Vignudelli, A.G. Kostianoy, P. Cipollini, and J. Benveniste, eds, Springer, New York.
- Ray, R.D., and G.T. Mitchum. 1996. Surface manifestation of internal tides generated near Hawaii. *Geophysical Research Letters* 23:2,101–2,104, <http://dx.doi.org/10.1029/96GL02050>.
- Ray, R.D., and G.T. Mitchum. 1997. Surface manifestation of internal tides in the deep ocean: Observations from altimetry and island gauges. *Progress in Oceanography* 40:135–162, [http://dx.doi.org/10.1016/S0079-6611\(97\)00025-6](http://dx.doi.org/10.1016/S0079-6611(97)00025-6).
- Ray, R.D., and E.D. Zaron. 2011. Non-stationary internal tides observed with satellite altimetry. *Geophysical Research Letters* 38, L17609, <http://dx.doi.org/10.1029/2011GL048617>.
- Simmons, H.L., R.W. Hallberg, and B.K. Arbic. 2004. Internal wave generation in a global baroclinic tide model. *Deep-Sea Research Part II* 51:3,043–3,068, <http://dx.doi.org/10.1016/j.dsr.2004.09.015>.
- St. Laurent, L., and C. Garrett. 2002. The role of internal tides in mixing the deep ocean. *Journal of Physical Oceanography* 32:2,882–2,899, [http://dx.doi.org/10.1175/1520-0485\(2002\)032<2882:TROITI>2.0.CO;2](http://dx.doi.org/10.1175/1520-0485(2002)032<2882:TROITI>2.0.CO;2).
- Tian, J., L. Zhou, and X. Zhang. 2006. Latitudinal distribution of mixing rate caused by the M2 internal tide. *Journal of Physical Oceanography* 36:35–42, <http://dx.doi.org/10.1175/JPO2824.1>.
- Wunsch, C. 1975. Internal tides in the ocean. *Reviews of Geophysics* 13:167–182, <http://dx.doi.org/10.1029/RG013i001p0167>.
- Zaron, E.D., C. Chavanne, G.D. Egbert, and P. Flament. 2009. Baroclinic tidal generation in the Kauai Channel inferred from high-frequency radio Doppler current meters. *Dynamics of Atmospheres and Oceans* 48(1–3):93–120, <http://dx.doi.org/10.1016/j.dynatmoce.2009.03.002>.
- Zhao, Z., and M.H. Alford. 2009. New altimetric estimates of mode-1 M2 internal tides in the central North Pacific Ocean. *Journal of Physical Oceanography* 39:1,669–1,684, <http://dx.doi.org/10.1175/2009JPO3922.1>.
- Zhao, Z., M.H. Alford, J. Girton, T.M.S. Johnston, and G.S. Carter. 2011. Internal tides around the Hawaiian Ridge estimated from multi-satellite altimetry. *Journal of Geophysical Research* 41, J12041, <http://dx.doi.org/10.1029/2011JC007045>.
- Zhao, Z., M.H. Alford, J.A. MacKinnon, and R. Pinkel. 2010. Long-range propagation of the semidiurnal internal tides from the Hawaiian Ridge. *Journal of Physical Oceanography* 40:713–736, <http://dx.doi.org/10.1175/2009JPO4207.1>.
- Zhao, Z., and E.A. D'Asaro. 2011. A perfect focus of the internal tide from the Mariana Arc. *Geophysical Research Letters* 38, L14609, <http://dx.doi.org/10.1029/2011GL047909>.